THE JOURNAL OF PHYSICAL CHEMISTRY C

pubs.acs.org/JPCC Article

Is Disorder Beneficial in Perovskite-Sensitized Solid-State Upconversion? The Role of DBP Doping in Rubrene

Published as part of The Journal of Physical Chemistry virtual special issue "Josef Michl Festschrift".

Sarah Wieghold,[‡] Alexander S. Bieber,[‡] Zachary A. VanOrman, Arianna Rodriguez, and Lea Nienhaus*

Cite This: *J. Phys. Chem. C* 2020, 124, 18132–18140 Read Online

ACCESS | Metrics & More | Article Recommendations | Supporting Information

ABSTRACT: Solid-state bulk lead halide perovskite thin films have recently shown progress as triplet sensitizers in infrared-to-visible photon upconversion (UC) schemes. Common systems pair lead halide perovskites with a rubrene annihilator, doped with ∼1% dibenzotetraphenylperiflanthene (DBP), to prevent the efficiency limiting process of singlet fission. However, the interplay between rubrene and DBP has not been investigated in these spin-coated bilayer systems. Here, we investigate the UC photoluminescence intensity and the dynamics of the triplet sensitization process as a function of the DBP doping percentage of rubrene, finding that, as a whole, DBP does not significantly affect the UC intensity of the lead halide perovskite sensitized scheme. This indicates that, in the solution-processed devices reported here, rubrene disorder is sufficient to suppress unwanted singlet fission processes, removing the requirement of an annihilator/emitter system.

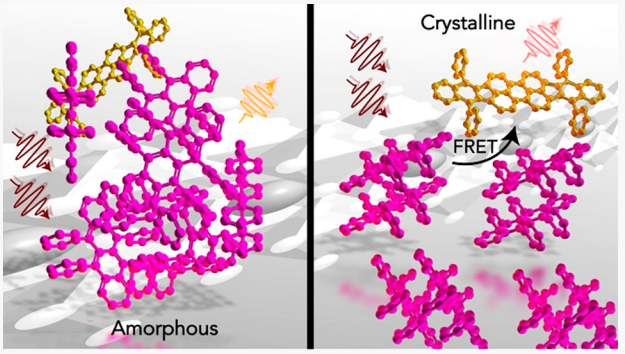

INTRODUCTION

Photon upconversion (UC), an anti-Stokes process capable of converting two incident photons to one photon higher in energy, has numerous applications in optoelectronics. Specifically, UC is of interest for applications in photocatalysis,[1−5] bioimaging,[6] displays,[7] sensing, and in photovoltaics.[8−11] The two latter of these applications call specifically for efficient infrared (IR)-to-visible UC, likely in the solid state. Triplet-triplet annihilation (TTA)-based UC offers one route toward efficient UC due to the longevity of triplet excited states.[12] The TTA-UC process results in an excited spin-singlet state from two spin-triplet states, where the relaxation of the excited spin-singlet state manifests itself as the UC emission. Because of spin-selection rules, however, organic annihilator molecules cannot be directly excited from their ground state to an excited triplet state. While both organometallics[12−18] and quantum-confined semiconductor nanocrystal materials[19−24] have been shown to be efficient triplet sensitizers, organometallics suffer from losses due to their high exchange energy, and semiconductor nanocrystals are surrounded by bulky organic ligands, which can limit efficient energy transfer within the inorganic layer and hinder efficient triplet energy transfer (TET) to the organic annihilator molecule.

Recently, we showed that lead halide perovskite thin films are capable of IR-to-visible UC under low solar-relevant fluences.[25−29] Specifically, we utilized a methylammonium formamidinium lead triiodide ($MAFAPbI_3$, or MAFA) thin film as the triplet sensitizer layer and a spin-coated rubrene doped with 1% dibenzotetraphenylperiflanthene (DBP) as the triplet annihilator layer. Because of the energetics of the triplet state, which is found at roughly half of the singlet energy, rubrene is capable of both TTA and its reverse process, singlet fission (SF).[30−32] Therefore, DBP has commonly been added to the rubrene layer in the solid state to rapidly harvest the singlet states from the annihilator rubrene, thus outcompeting SF.[19,33]

Previously, we placed our main focus on the role of the triplet sensitizer in perovskite-sensitized UC bilayer devices and the device fabrication technique.[25−29] We have been able to show that the UC process is dependent on both the sensitizer thickness,[28] as well as the triplet population and the resulting triplet diffusion length in the doped rubrene layer,[27] as well as the space charge region created at the perovskite/rubrene/DBP interface.[25]

However, currently, the direct role of the DBP dopant concentration in the rubrene annihilator layer on the UC efficiency has not been investigated in these solution-processed perovskite-sensitized devices. Previous reports by Wu et al.[19]

Received: June 10, 2020
Revised: July 21, 2020
Published: July 22, 2020

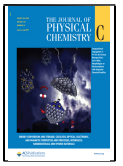

https://dx.doi.org/10.1021/acs.jpcc.0c05290
J. Phys. Chem. C 2020, 124, 18132−18140

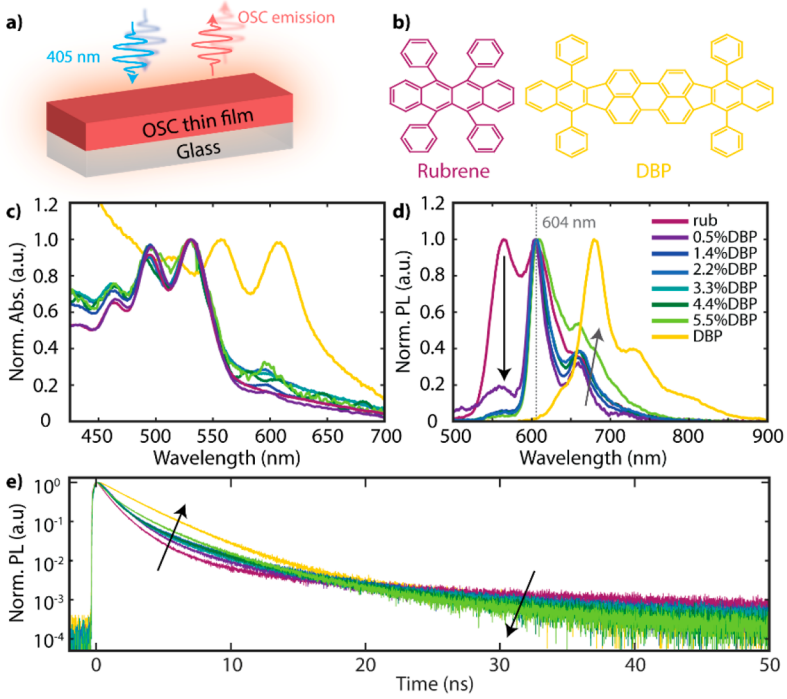

Figure 1. (a) Schematic of the OSC device. (b) Molecular structures of the OSCs: rubrene (purple) and DBP (yellow). (c) Absorption of the OSC devices with various amounts of the dopant dye DBP. (d) Steady-state emission spectra under 405 nm excitation of the OSC thin film devices. The gray arrow indicates the increase of the shoulder at ∼680 nm, indicating DBP aggregation. (e) PL lifetimes of the OSC films under 405 nm excitation. The early time component is elongated, and the delayed fluorescence is reduced (black arrows).

have shown an ∼19-fold increase in the upconverted emission intensity upon the addition of 0.5 wt % DBP to the rubrene layer and complete quenching of the rubrene emission at the cost of a red-shift of the emission of ∼40 nm or 0.15 eV. Interestingly, in contrast to these previous thermally evaporated bilayer UC devices, our solution-processed devices with ∼1 wt % DBP doping still often show strong emission at ∼565 nm, the wavelength of emission from the first vibronic feature of rubrene.[27] This indicates that the desired Förster resonance energy transfer (FRET) step from rubrene to the dopant dye DBP is not occurring to completion, allowing for a potential further improvement of the UC efficiency.

The question arises whether DBP is a desired and required guest in the solution-processed rubrene host, an unnecessary complication, or even a potentially unwanted parasite acting as a hole sink in the charge-transfer process. In the following, we seek to address these questions by comparing the dynamics of perovskite quenching attributed to triplet sensitization, the dynamics of the TTA-UC process, and the steady-state emission of the UC devices doped with different percentages of DBP.

EXPERIMENTAL METHODS

Device Fabrication. The glass substrates were first cleaned in 2% Hellmanex solution and sonicated for 15 min. Afterward, the substrates were cleaned in water and ethanol and sonicated for 15 min in the respective solution and wiped with acetone. The substrates were then placed in a UV ozone plasma cleaner (Ossila) for 15 min.

Methylammonium formamidinium triiodide (MAFA) perovskite thin films were prepared as described previously.[27] Briefly, a 1.2 M PbI_2 stock solution (99.99% TCI) was prepared in anhydrous dimethylformamide (DMF)/dimethyl sulfoxide (DMSO) 9:1 (v/v, Sigma-Aldrich). PbI_2 and methylammonium iodide (MAI) (1.2 M, Dyenamo) were mixed in a 1:1.09 molar ratio, and PbI_2 and formamidinium iodide (FAI) (1.2 M, Dyenamo) were mixed in a 1:1.09 molar ratio. To achieve an ∼100 nm thick MAFA film, the final precursor concentration was diluted twofold in DMF/DMSO 9:1 (v/v). For the perovskite film deposition, a two-step spin-coating program was used: 1000 rpm for 10 s and 5000 rpm for 30 s. Anhydrous chlorobenzene (Sigma-Aldrich) was dropped onto the substrate as antisolvent. Afterward, the films were annealed at 100 °C for 10 min in the glovebox.

Rubrene (99.99%) and DBP (98% high-performance liquid chromatography (HPLC)) were purchased from Sigma-Aldrich and used as received. A 10 mg/mL rubrene solution was prepared in anhydrous toluene and doped with DBP (10 mg/mL in anhydrous toluene) at different ratios: 0.5%, 1.4%, 2.2%, 3.3%, 4.4%, and 5.5%. The rubrene/DBP solutions were then spin-coated onto a bare glass substrate or onto the MAFA perovskite layer at 6000 rpm for 20 s. To prevent oxygen infiltration all films were sealed with a coverslip using a two-part epoxy (Devcon) under nitrogen atmosphere.

Optical Characterization. *Steady State.* A UV−vis spectrometer (Shimadzu UV-2450) was used to measure the absorption of the films and bilayer devices. The steady-state photoluminescence (PL) was measured with an OceanOptics spectrometer (HR2000+ES) under continuous-wave excitation at 405 nm (PicoQuant LDH-D-C-405) and 780 nm (PicoQuant LDH-D-C-780). For comparison with the solid bilayer devices, we also measured the absorption and PL of 10 mg/mL rubrene in toluene and 10 mg/mL DBP in toluene (Supporting Information).

Time Resolved. The time-resolved PL lifetimes were measured by means of time-correlated single photon counting

https://dx.doi.org/10.1021/acs.jpcc.0c05290
J. Phys. Chem. C 2020, 124, 18132−18140

(TCSPC) using a single-photon avalanche photodiode (Micro Photon Devices) and a HydraHarp 400 or a MultiHarp 150 (PicoQuant). The photon arrival times were measured by focusing the emission onto the detector using reflective optics. The lifetimes of rubrene/DBP with varying ratios in solution or supported on the bare glass substrate were measured under 405 nm excitation equipped with a 425 nm long-pass filter (Chroma Tech) to remove excess laser scatter. The MAFA decay dynamics was measured under pulsed 780 nm excitation at a repetition rate of 31.25 kHz (4.1 μW) using an 800 nm long-pass filter (Thorlabs). The upconverted dynamics was measured under 780 nm excitation at a repetition rate of 31.25 kHz (4.1 μW) and an average power using a 600/40 nm (center/width) band-pass filter (Thorlabs). To measure the incident laser beam power, a silicon power meter (Thorlabs PM100-D) was used.

Time-Resolved Emission Spectra. Time-resolved emission spectra were collected using a Gemini interferometer (NIREOS). For the organic semiconductor (OSC) thin films, the time-resolved emission spectra (TRES) were recorded over 175 steps with a collection time of 5001 ms at each step. For the MAFA/rubDBP devices, the time resolution was set to 128 ps. The TRES were recorded over 250 steps with a collection time of 10 001 ms at each step. A 405 nm picosecond pulsed laser diode (PicoQuant LDH-D-C-405) was used as an excitation source at 10 MHz, a power density of 2.7 W/cm^2 was used for the OSC thin films and at 250 kHz, and a power density of 36 mW/cm^2 was used for the MAFA/rubDBP devices. A 425 nm long-pass filter (Chroma Tech.) was used to remove the excess laser scatter. Photon arrival times were collected via a HydraHarp 400 (PicoQuant) event timer connected to a silicon single-photon avalanche photodiode (Micro Photon Devices).

X-ray Diffraction. X-ray diffraction patterns were taken using a Rigaku SmartLab X-ray diffractometer equipped with CBO-α optics and a D/teX Ultra 2 silicon strip detector. A Cu Kα source (k = 1.5406 Å) was operated at 44 mA and 40 kV to acquire the pattern with a step size of 0.05°, slit width of 0.5, and a scan rate of 4°/min.

RESULTS AND DISCUSSION

We begin by investigating the properties of the OSC layer composed of rubrene and varying the amounts of DBP without the perovskite sensitizer to establish the effect of doping on the organic layer. Figure 1a is a schematic of the OSC thin film on glass; Figure 1b highlights the chemical structures of both the annihilator dye rubrene, as well as the dopant dye DBP. In Figure 1c, the absorbance of the films is shown, which is dominated by the rubrene absorption highlighting the low doping concentration of DBP investigated: 0−5.5%. The absolute absorbance of the DBP-only film is fairly low, which can be attributed to the low solubility of DBP in toluene, and a resulting thinner film (compare Supporting Information Figure S1), as well as poor adhesion to the glass substrate. Figure 1d highlights the change of the emission profile of the OSC films. The rubrene-only film shows the expected emission feature at ∼565 nm, as well as a further strong vibronic feature at ∼604 nm, a clear indication of the existence of small (crystalline) aggregates. With increasing DBP doping, we see the expected trend, as reported by Kazlauskas and co-workers.[34] The peak at 565 nm attributed to the emission of the first vibronic feature of rubrene decreases and then becomes negligible at higher DBP doping concentrations. An increasing emission stemming from isolated DBP molecules centered at 605 nm is observed, with a slight red shift of the peak with increasing DBP concentration (compare Supporting Information S2 for characterization of the organic dyes in solution). The DBP-only film shows even further red-shifted emission, indicating that close packing of the DBP molecules disfavors certain vibronic transitions and that the interactions influence the emission wavelength. The increasing low-energy shoulder observed in the PL (gray arrow) of high DBP doping concentration in our rubrene films therefore indicates that there is phase segregation occurring in the films. We are not finding a homogeneous film at high DBP concentrations of 5.5%; rather, there are small DBP aggregates within the doped rubrene film. Therefore, we annotated this concentration with a red asterisk in the following, as its behavior is often comparable to a lower DBP concentration. Figure 1e shows the PL decay dynamics of the OSC films under pulsed 405 nm excitation at a repetition rate of 2.5 MHz. As expected, the solid-state rubrene films show a fast decay attributed to SF and spontaneous PL, followed by a longer tail due to delayed fluorescence stemming from TTA-UC. As the concentration of DBP is increased, the amount of FRET is increased, and the early time component is elongated. This is consistent with an increased singlet lifetime resulting from increased emission from DBP and a reduced amount of nonradiative relaxation due to SF and other possible pathways. The delayed component is concurrently reduced, as less long-lived triplet states are created by the undesired SF process (compare Supporting Information Table S1).

We observe that the OSC layer behaves as expected and that only a minimal amount of emission from the first vibronic feature of rubrene can be observed at optimum doping levels close to 1% (compare Table 1). However, in our previous reports of perovskite/OSC bilayer devices, we observed relatively strong emission at 565 nm, despite the addition of ∼1% DBP.[27]

Table 1. Relative Quenching Ratio[a]

	OSC: PL at ∼565 nm		bilayer: PL at ∼565 nm	
DBP doping (%)	I_{rub}/I_{doped}	η_{FRET}	I_{rub}/I_{doped}	η_{FRET}
0		0%		0%
0.5	0.16	84%	0.16	84%
1.4	0.083	92%	0.071	93%
2.2	0.069	93%	0.081	92%
3.3	0.068	93%	0.069	93%
4.4	0.049	95%	0.065	93%
5.5	0.025*	98%*	0.095*	90%*

[a]Relative quenching ratio of the rubrene peak emission at ∼565 nm under direct excitation (405 nm) of the OSC in the OSC-only and MAFArub bilayer devices, and the corresponding calculated FRET efficiency η_{FRET}.

In the following, we investigate the properties of the bilayer UC devices in more detail. We fabricate several UC devices based on methylammonium formamidinium lead triiodide perovskite ($MA_{0.85}FA_{0.15}PbI_3$, MAFA) thin films and a subsequent layer of the differently doped rubrene layers ranging between 0 and 5.5% DBP. The UC devices (MAFA/rubDBP) with varying DBP concentrations are specifically referred to as MAFArub (0% DBP) and MAFA/x%DBP (x = 0.5−5.5). The absorbance of the bilayer films is highlighted in Figure 2a, showing the expected sharp absorption onset at

https://dx.doi.org/10.1021/acs.jpcc.0c05290
J. Phys. Chem. C 2020, 124, 18132−18140

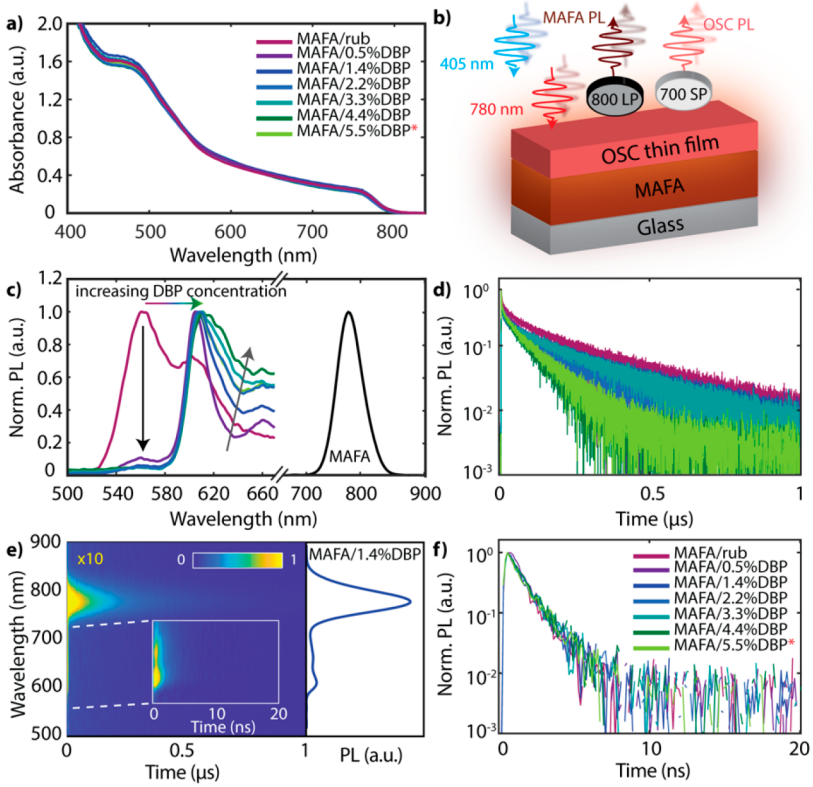

Figure 2. (a) Absorbance spectra of the MAFA/rub films doped with varying DBP percentages. (b) Schematic of the device architecture: both 405 and 780 nm excitation result in OSC and MAFA emission. (c) Steady-state emission spectra under 405 nm excitation of the MAFA/rubDBP devices. The OSC emission is shown on the left, and the perovskite emission is shown on the right (black). (d) PL dynamics of the MAFA/rubDBP films under 405 nm excitation at an incident power of 7.1 μW and a repetition frequency of 250 kHz. The lifetimes were integrated over a spectral region from 760 to 810 nm from the TRES in (e). (e) Time-resolved emission map for the MAFA/1.4%DBP film (left) and the normalized integrated emission spectra (right). The map was collected under 405 nm excitation at a repetition frequency of 250 kHz. (f) PL dynamics from 550 to 650 nm extracted from the TRES maps.

~780 nm, corresponding to the optical bandgap of this MAFA composition (~1.6 eV). The bilayer device structure is shown in the schematic in Figure 2b. As previously observed, the absorbance spectrum is dominated by the strong MAFA absorption, and the distinct vibronic features of the absorption of the thin organic layer are not distinguishable. The emission spectra of the bilayer devices with different DBP dopant concentrations under direct 405 nm excitation are shown in Figure 2c. The MAFA emission at 780 nm is independent of the addition of the organic layer (compare Figure S3). Similar to the OSC layers, under 405 nm excitation we observe a reduction of the rubrene vibronic feature at 565 nm and a slight red shift of the DBP emission peak with increasing DBP concentration, as well as a broadening of the second vibronic feature due to molecular aggregation. However, in contrast to the OSC-only films, the increase of the red-shifted PL is more pronounced (gray arrow). Interestingly, we also find an obvious difference in the shape of the PL spectrum for the undoped rubrene layer deposited on the MAFA thin film compared to the OSC-only film: the intensity of the second vibronic feature is reduced in comparison to the OSC-only film, possibly indicating an even more disordered film (compare Figure S4 for X-ray diffraction highlighting the amorphous nature of the OSC). On the hydrophilic glass substrate used in the OSC-only films, the tetracene backbone of rubrene is expected to arrange upright at an angle to the surface, while the strong π-cation interactions between MA^+ and rubrene will result in rubrene laying nearly flat on the perovskite surface.[35] As a result, the solution-cast OSC layers may form in a different manner depending on the underlying substrate, and the varying intermolecular interactions can yield different allowed transitions.

Figure 2d shows the perovskite PL dynamics of the varying bilayer devices under 405 nm pulsed excitation obtained in the spectral range of 760−810 nm (compare Figure S5a for the MAFA-only lifetime). The decay shows the typical behavior of perovskite films at low fluences: a rapid early time quenching attributed to trap-state filling or hot-carrier cooling, as well as a long-lived decay due to nongeminate carrier recombination. Interestingly, we observe a decrease in the PL lifetime with increasing DBP concentration (compare Figure S5b for the MAFA-only lifetime under 780 nm excitation). The underlying cause is not clear; several possibilities include: (i) energetically allowed hole extraction to DBP, (ii) reduced passivation by rubrene, or (iii) less optical absorption by the overlying OSC layer due to the red-shifted absorption of DBP, resulting in a higher effective fluence absorbed by the perovskite.

The time-resolved emission spectrum (TRES) map of a representative bilayer device (1.4% DBP) is shown in Figure 2e (compare Figures S6 and S7 for the other TRES maps and integrated spectra and see Figure S8 for additional information). The slow emission dynamics of the MAFA component is clearly seen in comparison to the rapid emission of the organic layer, which is fully decayed after ~10 ns (compare inset). The time-integrated wavelength-resolved spectrum is shown on the right. Within the measurement

https://dx.doi.org/10.1021/acs.jpcc.0c05290
J. Phys. Chem. C 2020, 124, 18132−18140

uncertainty of the extracted lifetimes, no differences in the decay dynamics are observed; rather, all OSC compositions exhibit similar lifetimes (Figure 2f).

By comparing the residual intensity of the first vibronic emission feature of rubrene at 565 nm in the doped films I_{doped} to the undoped rubrene emission intensity I_{rub} under direct excitation at 405 nm, we can estimate the FRET efficiency between rubrene and DBP of the fabricated OSC films (Figure 1d) and our MAFA-based UC devices (Figure 2c). Table 1 indicates the relative quenching ratio $\frac{I_{rub}}{I_{doped}}$, which reflects the quality of the FRET process in our OSC films and MAFA/rubDBP bilayer devices at different doping concentrations. As expected, we observe a decrease in the relative intensity of rubrene's first vibronic feature with increasing DBP doping concentration and, therefore, an overall increase in the FRET efficiency $\eta_{FRET}=1-\frac{I_{rub}}{I_{doped}}$ from rubrene to DBP. FRET can only occur if rubrene and DBP are within several nanometers of each other and oriented favorably; hence, we speculate that the addition of more DBP reduces the average excited rubrene-DBP distance and, therefore, more efficient FRET can occur under direct 405 nm excitation.

As the main goal of this study is to elucidate the effect of the DBP concentration on the overall performance of the MAFA/rubDBP UC devices, we investigate the upconverted emission intensity for all DBP doping concentrations. Figure 3a depicts a box plot of the obtained UC PL intensity integrated from 500 to 700 nm to account for the changes in the spectral shape for DBP doping percentages of 0−5.5% under 780 nm excitation (UC PL intensity was taken at seven different spots across the films for statistics; compare Supporting Information Figure S9 for the single emission spectra). We find that, within error, all doping concentration yield similar UC PL intensities.

The UC efficiency η_{UC} (eq 1) is defined as the product of intersystem crossing (ISC) η_{ISC}, the triplet energy transfer from the sensitizer to the annihilator η_{TET}, and the TTA efficiency η_{TTA}. It is often normalized by the annihilator quantum yield (QY) η_{ann}.[12,36,37] In bulk perovskite-sensitized UC, the triplet sensitization mechanism involves transfer of rapidly spin-mixing free carriers and removes the requirement of ISC. As a result, the UC efficiency simplifies to

$$\eta_{UC} = \eta_{TET}\eta_{TTA}\eta_{ann} \quad (1)$$

To remove any influence of the underlying annihilator QY, in Figure 3b the integrated UC intensity is shown normalized by the average integrated rubrene/DBP PL intensity under 405 nm excitation (compare also Supporting Information Figure S10).

As mentioned previously, the DBP addition has previously been shown to result in a 19-fold increase in the observed upconverted emission for vapor-deposited UC devices.[19] Interestingly, we do not observe the same strong influence of the UC PL obtained in our measurements. We observe that, within measurement error, the DBP concentration does not appear to affect the upconverted PL intensity or the underlying OSC PL intensity under direct excitation.

To further investigate the role of DBP on the UC PL intensity, we investigate the time-resolved PL dynamics of both the MAFA sensitizer (Figure 4a) as well as the obtained UC dynamics (Figure 4b). We find the typical behavior for the MAFA PL in all of our bilayer devices: rapid quenching followed by an elongation of the PL dynamics at later times, due to singlet back-transfer after successful TTA-UC,[28] and a

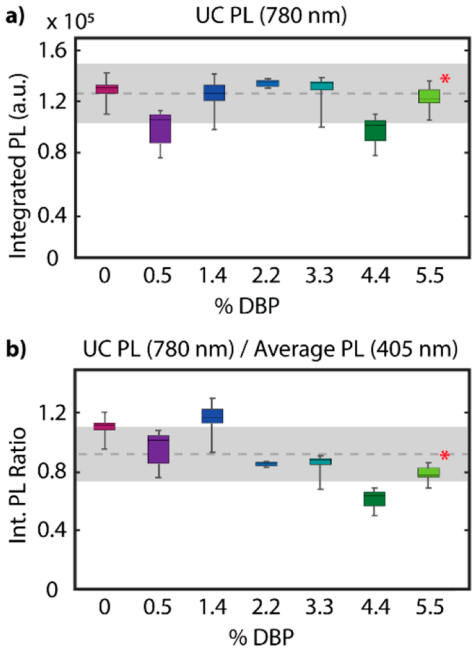

Figure 3. Box plots of the integrated PL intensities from 500 to 700 nm of seven different spots on various films with varying DBP doping percentages. The "whiskers" show the range of the data, while the line gives the median. (a) UC PL emission intensities of the various doping concentrations under 780 nm excitation. The dashed gray line shows the average integrated PL intensity, while the gray box indicates the range of uncertainty based on the whiskers. (b) The UC PL intensities shown in (a) normalized by the average integrated PL intensity under 405 nm excitation (compare Supporting Information Figure S10).

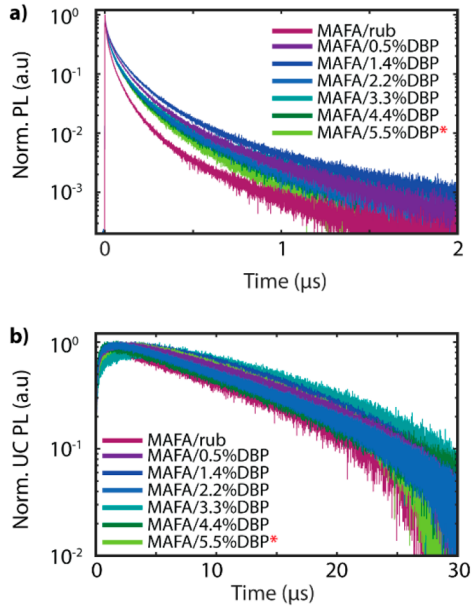

Figure 4. PL dynamics of the MAFA/rubDBP films under 780 nm excitation at 31.25 kHz and a power density of 21 mW/cm^2. (a) PL decay dynamics of the MAFA perovskite emission (>800 nm). (b) UC PL dynamics of the MAFA/rubDBP samples, showing the typical rise and fall of the upconverted PL.

https://dx.doi.org/10.1021/acs.jpcc.0c05290
J. Phys. Chem. C 2020, 124, 18132−18140

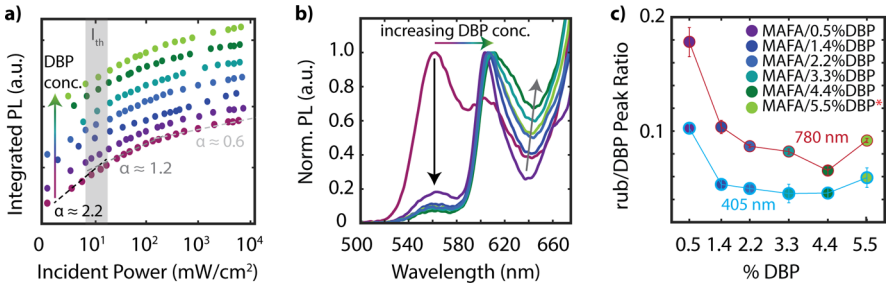

Figure 5. (a) Log–Log plot of the UC PL intensity (integrated over 20 s) as a function of the incident laser power density. The curves are offset for clarity and therefore are not an indication of the absolute PL intensity. The dashed lines are added to guide the eye to the observed slope changes. The gray shaded region highlights the uncertainty region of the extracted I_{th} values. (b) Steady-state emission spectra of the UC PL emission of the MAFA/rubDBP samples under 780 nm excitation. The black arrow highlights the decrease of the rubrene PL at 565 nm, and the gray and blue-green arrow highlight the increasing red-shift of the upconverted PL. (c) Ratio of the rubrene/DBP emission peak maxima at ~560 and 605 for the MAFA/rubDBP samples under 405 nm excitation (blue outline) and 780 nm excitation (red outline).

reduction in the carrier density due to charge extraction. No obvious correlation (within spot-to-spot variations due to sample inhomogeneities) is observed between the PL dynamics and the DBP concentration, indicating that DBP is not a critical factor here. The UC PL dynamics is also very similar across all doping concentrations investigated. Within the sample-to-sample and spot-to-spot variations stemming from slight inhomogeneities across the sample, we conclude that DBP plays no role in the carrier transfer, triplet sensitization, or TTA process (compare Supporting Information Figure S11 for a variation of UC PL dynamics found for MAFArub. The variation in dynamics observed spans the range of dynamics found here for all dopant concentrations). This result is not unexpected, as the rubrene/DBP system is meant to simply be an annihilator/emitter system. As a result, rubrene dictates the TTA-UC properties, and DBP simply emits the singlets created in rubrene.

Lastly, we investigate the upconverted emission under steady-state illumination conditions. Figure 5a shows the upconverted emission as a function of the incident power density. The resulting curves are offset for visualization purposes and, therefore, are not directly correlated to the brightness of a sample (also compare Figure 3a). The power dependence of TTA-UC is unique: at low power, TTA is inefficient, and therefore, the triplet decay is dominated by other decay pathways, leading to a quadratic dependency of the UC PL on the incident power. At higher powers, above the so-called efficiency threshold I_{th}, this quadratic relationship gives way to a linear dependency. Above the intensity threshold, UC becomes efficient, and the predominant triplet decay pathway becomes TTA, leading to the observed linear relationship. Nongeminate free carrier sensitization of the triplet state further complicates the relationship between the incident power and the upconverted PL intensity, as the perovskite exhibits a nonlinear power dependency with a slope $1 < \beta < 2$. We have previously shown that this further influences the UC PL intensity dependence, resulting in an observed slope change from $\alpha = 2\beta$ to $\alpha = \beta$ at the intensity threshold.[28]

As expected, on the basis of our results thus far, we observe that the power dependence of the UC PL intensity is independent of the DBP doping concentration. In agreement with our previous results, we obtain a value $I_{th} \approx 10$ mW/cm^2 for all bilayer devices. Figure 5b shows the normalized upconverted PL spectra under 780 nm excitation for the bilayer devices fabricated with the different DBP doping concentrations. We observe the same behavior as under direct 405 nm excitation: a red shift of the PL peak intensity, as well as an increase in the emission intensity from the second vibronic feature, indicating aggregation of DBP. For the DBP-doped samples, one major difference becomes obvious: the quenching of the rubrene emission is not as pronounced as observed under direct 405 nm excitation. As we cannot directly compare the quenching of the rubrene emission feature in the presence of the DBP acceptor across doping concentrations, we instead focus on the ratio of the rubrene and DBP emission. In Figure 5c we plot the ratio of the first vibronic feature of rubrene at 565 nm and the first vibronic feature of DBP at 605 nm under both direct 405 nm excitation, as well as the 780 nm excitation, which results in the upconverted PL. The expected monotonic decrease of the ratio up to 4.4% DBP doping is found, indicating an increase in FRET efficiency, followed by a slight increase in the ratio due to the inhomogeneities resulting from DBP agglomeration in the highest doping concentration of 5.5%. We observe that this ratio is higher for the upconverted PL than for the direct emission, which indicates that the FRET efficiency η_{FRET} is lower under 780 nm excitation than under 405 nm excitation (compare Table 2).

Table 2. Relative Quenching Ratio[a]

	UC PL at 565 nm	
DBP doping (%)	I_{rub}/I_{doped}	η_{FRET}
0		0%
0.5	0.22	78%
1.4	0.12	88%
2.2	0.10	90%
3.3	0.09	91%
4.4	0.05	95%
5.5	0.10	90%

[a]Relative quenching ratio of the rubrene emission at 565 nm under 780 nm excitation resulting in TTA-UC and the calculated FRET efficiency η_{FRET}.

This result is unexpected, as the FRET efficiency between rubrene and DBP should not be influenced by the process resulting in the excited singlet state in rubrene. Therefore, we can summarize a key observation in the MAFA/rubDBP UC devices investigated here: A different subpopulation of rubrene molecules must be undergoing TTA-UC and emitting the upconverted PL than is emitting under direct 405 nm excitation.

https://dx.doi.org/10.1021/acs.jpcc.0c05290
J. Phys. Chem. C 2020, 124, 18132–18140

However, we found no indication that DBP significantly enhances the intensity of the upconverted emission in our solution-fabricated perovskite-sensitized UC devices. As expected, our time-resolved PL spectroscopy shows that DBP does not play a role in the triplet sensitization or UC mechanism; rather, DBP acts only as a singlet sink after TTA has occurred to avoid SF. Typical aggregation-induced effects can be observed for DBP concentrations above ∼1%, resulting in a visible red-shift of the DBP emission, thus further reducing the energy gained by UC. This would indicate that the addition of DBP, especially at high concentrations, and the resulting 0.15 eV energy loss due to FRET do more harm than good in these solution-fabricated devices.

In the following, we will discuss why these results are in contrast to previous reports.[19,23] Other publications report a strong dependence of the upconverted PL intensity on the addition of DBP, while it does not appear to be a crucial factor here. One of the major differences is the processing condition of the OSC layer. In previous PbS quantum dot-based UC devices, the doped organic layer was codeposited by thermal evaporation, while we are using solution processing to fabricate our OSC layer. Vapor deposition commonly results in crystalline rubrene films, where the individual rubrene molecules are aligned in an orthorhombic crystal structure.[38] Because of this long-range order allowing for the delocalization of the rubrene singlet state, these films are primed for rapid SF to occur. In these studies, it was shown that DBP is a requirement to harvest the singlets prior to rapid SF in rubrene.

As shown in our previous studies,[26] the solution processing of the OSC layer results in a combination of both amorphous as well as small crystalline regions. Fully amorphous rubrene layers have been shown to exhibit no SF due to the lack of a long-range order in the OSC film,[39] and they have a PL lifetime similar to rubrene in solution. On the basis of our emission spectra, time-resolved PL dynamics, and surface morphologies,[26,28] we conclude that both crystalline and amorphous regions of rubrene are present in our films. A certain amount of molecular alignment within the rubrene layer will also be required for TTA-UC to occur, which we are clearly observing. Changing the rubrene crystallinity from polycrystalline to amorphous has been shown to reduce the rate of SF 10-fold, as the excitons cannot delocalize in the same manner with lack of long-range order, thus slowing the SF process.[32,40] However, because of their very long lifetimes (∼100 μs),[41] triplets can diffuse over long distances throughout the amorphous rubrene film to find properly aligned molecules for TTA-UC. Employing fluorescence lifetime imaging microscopy (FLIM), we have previously been able to observe that the crystalline aggregates of rubrene do not exhibit strong UC PL,[26] likely due to rapid SF occurring—further supporting our hypothesis that the unusually high UC observed in rubrene-only UC devices in comparison to the DBP-doped counterparts is due to the reduced amounts of SF in the amorphous films presented here.

Lastly, we give a short discussion on the role of DBP and a probable cause of the unusual effects found for the higher DBP concentrations. DBP is only poorly soluble in toluene, and it is therefore likely that small DBP aggregates form, which can act as nucleation centers for crystalline rubrene agglomerates. As a result, the overall properties of such an upconversion device is more similar to a lower concentration, as DBP agglomerates will reduce the amount of DBP dispersed throughout the OSC. The band alignment allows for hole transfer to occur from MAFA to DBP. However, the triplet state is not accessible. In this case, DBP could act as a hole sink, and excited-state triplet or singlet deactivation pathways including exciton-hole annihilation are feasible, which may result in a reduced (UC) PL QY at high DBP concentrations.

CONCLUSION

In summary, we have investigated the dependence of the UC PL intensity, as well as the triplet sensitization and UC mechanism, on the DBP doping concentration in rubrene. In contrast to previous reports, which show an ∼19-fold increase in the UC PL upon DBP addition,[19] we find very little change in the observed UC PL intensity for the amorphous solution-processed films investigated here. However, the addition of DBP red-shifts the UC emission by ∼0.15 eV, thus reducing the energy gained in the UC process. We attribute the reduced influence of SF in our solution-processed devices to the lack of long-range order in the created amorphous rubrene film, which reduces the rate of SF. Within measurement uncertainty, all of our solution-processed devices exhibit the same amount of UC emission, indicating that further work on film reproducibility, film homogeneity, and a more controlled fabrication technique may be required to fully harvest the full potential of these devices.

ASSOCIATED CONTENT

Supporting Information

The Supporting Information is available free of charge at https://pubs.acs.org/doi/10.1021/acs.jpcc.0c05290.

Lifetime fit calculations, integrated photoluminescence calculation, detector external quantum efficiency and supplemental figures: amplitudes, lifetimes, and amplitude-weighted average lifetimes from the OSC only films; OSC thin film UV−vis absorbance; OSC solution characterization; MAFA/OSC integrated PL emission; X-ray diffraction; PL decay dynamics for MAFA; integrated PL spectra and TRES of the OSC thin films; integrated PL spectra and TRES of the MAFA/OSC thin films; detector external quantum efficiency influence; upconverted PL in seven different locations for the MAFA/OSC films; box plots of the integrated PL from the seven different UC locations; upconverted PL dynamics of MAFA/rub (PDF)

AUTHOR INFORMATION

Corresponding Author

Lea Nienhaus − *Department of Chemistry and Biochemistry, Florida State University, Tallahassee, Florida 32306, United States;* orcid.org/0000-0003-1412-412X; Email: lnienhaus@fsu.edu

Authors

Sarah Wieghold − *Department of Chemistry and Biochemistry, Florida State University, Tallahassee, Florida 32306, United States*

Alexander S. Bieber − *Department of Chemistry and Biochemistry, Florida State University, Tallahassee, Florida 32306, United States*

Zachary A. VanOrman − *Department of Chemistry and Biochemistry, Florida State University, Tallahassee, Florida 32306, United States*

https://dx.doi.org/10.1021/acs.jpcc.0c05290
J. Phys. Chem. C 2020, 124, 18132−18140

Arianna Rodriguez − *Department of Chemistry and Biochemistry, Florida State University, Tallahassee, Florida 32306, United States*

Complete contact information is available at: https://pubs.acs.org/10.1021/acs.jpcc.0c05290

Author Contributions

‡(S.W. and A.S.B.) These authors contributed equally

Notes

The authors declare no competing financial interest.

■ ACKNOWLEDGMENTS

The authors gratefully acknowledge Florida State University for funding. We also thank the National Science Foundation (NSF)-Research Experiences for Undergraduates (REU) Sites program. This material is based upon work supported by the NSF under Grant No. CHE-1659661. We thank the Mattoussi group at Florida State University for the use of their UV−vis spectrometer. We thank N. Bertone (PicoQuant) for the opportunity to demo the Gemini interferometer and A. Perri and F. Preda (NIREOS) for their support with the Gemini.

■ REFERENCES

(1) Zhou, J.; Liu, Q.; Feng, W.; Sun, Y.; Li, F. Upconversion Luminescent Materials: Advances and Applications. *Chem. Rev.* **2015**, *115*, 395−465.
(2) Ravetz, B. D.; Pun, A. B.; Churchill, E. M.; Congreve, D. N.; Rovis, T.; Campos, L. M. Photoredox Catalysis Using Infrared Light via Triplet Fusion Upconversion. *Nature* **2019**, *565*, 343−346.
(3) Pfund, B.; Steffen, D. M.; Schreier, M. R.; Bertrams, M.-S.; Ye, C.; Börjesson, K.; Wenger, O. S.; Kerzig, C. UV Light Generation and Challenging Photoreactions Enabled by Upconversion in Water. *J. Am. Chem. Soc.* **2020**, *142*, 10468−10476.
(4) Khnayzer, R. S.; Blumhoff, J.; Harrington, J. A.; Haefele, A.; Deng, F.; Castellano, F. N. Upconversion-Powered Photoelectrochemistry. *Chem. Commun.* **2012**, *48*, 209−211.
(5) Barawi, M.; Fresno, F.; Pérez-Ruiz, R.; de la Peña O'Shea, V. A. Photoelectrochemical Hydrogen Evolution Driven by Visible-to-Ultraviolet Photon Upconversion. *ACS Appl. Energy Mater.* **2019**, *2*, 207−211.
(6) Zhang, K. Y.; Zhang, T.; Wei, H.; Wu, Q.; Liu, S.; Zhao, Q.; Huang, W. Phosphorescent Iridium(III) Complexes Capable of Imaging and Distinguishing between Exogenous and Endogenous Analytes in Living Cells. *Chem. Sci.* **2018**, *9*, 7236−7240.
(7) Deng, R.; Qin, F.; Chen, R.; Huang, W.; Hong, M.; Liu, X. Temporal Full-Colour Tuning through Non-Steady-State Upconversion. *Nat. Nanotechnol.* **2015**, *10*, 237−242.
(8) Schulze, T. F.; Schmidt, T. W. Photochemical Upconversion: Present Status and Prospects for Its Application to Solar Energy Conversion. *Energy Environ. Sci.* **2015**, *8*, 103−125.
(9) Trupke, T.; Green, M. A.; Würfel, P. Improving Solar Cell Efficiencies by Up-Conversion of Sub-Band-Gap Light. *J. Appl. Phys.* **2002**, *92*, 4117−4122.
(10) Meng, F.-L.; Wu, J.-J.; Zhao, E.-F.; Zheng, Y.-Z.; Huang, M.-L.; Dai, L.-M.; Tao, X.; Chen, J.-F. High-Efficiency near-Infrared Enabled Planar Perovskite Solar Cells by Embedding Upconversion Nanocrystals. *Nanoscale* **2017**, *9*, 18535−18545.
(11) He, M.; Pang, X.; Liu, X.; Jiang, B.; He, Y.; Snaith, H.; Lin, Z. Monodisperse Dual-Functional Upconversion Nanoparticles Enabled Near-Infrared Organolead Halide Perovskite Solar Cells. *Angew. Chem., Int. Ed.* **2016**, *55*, 4280−4284.
(12) Singh-Rachford, T. N.; Castellano, F. N. Photon Upconversion Based on Sensitized Triplet−Triplet Annihilation. *Coord. Chem. Rev.* **2010**, *254*, 2560−2573.
(13) Islangulov, R. R.; Kozlov, D. V.; Castellano, F. N. Low Power Upconversion Using MLCT Sensitizers. *Chem. Commun.* **2005**, *30*, 3776−3778.
(14) Islangulov, R. R.; Lott, J.; Weder, C.; Castellano, F. N. Noncoherent Low-Power Upconversion in Solid Polymer Films. *J. Am. Chem. Soc.* **2007**, *129*, 12652−12653.
(15) Fan, C.; Wei, L.; Niu, T.; Rao, M.; Cheng, G.; Chruma, J. J.; Wu, W.; Yang, C. Efficient Triplet−Triplet Annihilation Upconversion with an Anti-Stokes Shift of 1.08 eV Achieved by Chemically Tuning Sensitizers. *J. Am. Chem. Soc.* **2019**, *141*, 15070−15077.
(16) Haefele, A.; Blumhoff, J.; Khnayzer, R. S.; Castellano, F. N. Getting to the (Square) Root of the Problem: How to Make Noncoherent Pumped Upconversion Linear. *J. Phys. Chem. Lett.* **2012**, *3*, 299−303.
(17) Schmidt, T. W.; Castellano, F. N. Photochemical Upconversion: The Primacy of Kinetics. *J. Phys. Chem. Lett.* **2014**, *5*, 4062−4072.
(18) Amemori, S.; Sasaki, Y.; Yanai, N.; Kimizuka, N. Near-Infrared-to-Visible Photon Upconversion Sensitized by a Metal Complex with Spin-Forbidden yet Strong S0−T1 Absorption. *J. Am. Chem. Soc.* **2016**, *138*, 8702−8705.
(19) Wu, M.; Congreve, D. N.; Wilson, M. W. B.; Jean, J.; Geva, N.; Welborn, M.; Van Voorhis, T.; Bulović, V.; Bawendi, M. G.; Baldo, M. A. Solid-State Infrared-to-Visible Upconversion Sensitized by Colloidal Nanocrystals. *Nat. Photonics* **2016**, *10*, 31−34.
(20) Okumura, K.; Mase, K.; Yanai, N.; Kimizuka, N. Employing Core-Shell Quantum Dots as Triplet Sensitizers for Photon Upconversion. *Chem. - Eur. J.* **2016**, *22*, 7721−7726.
(21) Han, Y.; He, S.; Luo, X.; Li, Y.; Chen, Z.; Kang, W.; Wang, X.; Wu, K. Triplet Sensitization by "Self-Trapped" Excitons of Nontoxic CuInS2 Nanocrystals for Efficient Photon Upconversion. *J. Am. Chem. Soc.* **2019**, *141*, 13033−13037.
(22) VanOrman, Z. A.; Bieber, A. S.; Wieghold, S.; Nienhaus, L. Green-to-Blue Triplet Fusion Upconversion Sensitized by Anisotropic CdSe Nanoplatelets. *Chem. Mater.* **2020**, *32*, 4734−4742.
(23) Nienhaus, L.; Wu, M.; Geva, N.; Shepherd, J. J.; Wilson, M. W. B.; Bulović, V.; Van Voorhis, T.; Baldo, M. A.; Bawendi, M. G. Speed Limit for Triplet-Exciton Transfer in Solid-State PbS Nanocrystal-Sensitized Photon Upconversion. *ACS Nano* **2017**, *11*, 7848−7857.
(24) Mase, K.; Okumura, K.; Yanai, N.; Kimizuka, N. Triplet Sensitization by Perovskite Nanocrystals for Photon Upconversion. *Chem. Commun.* **2017**, *53*, 8261−8264.
(25) Wieghold, S.; Nienhaus, L. Precharging Photon Upconversion: Interfacial Interactions in Solution-Processed Perovskite Upconversion Devices. *J. Phys. Chem. Lett.* **2020**, *11*, 601−607.
(26) Wieghold, S.; Bieber, A. S.; Lackner, J.; Nienhaus, K.; Nienhaus, G. U.; Nienhaus, L. One-Step Fabrication of Perovskite-Based Upconversion Devices. *ChemPhotoChem* **2020**. DOI: 10.1002/cptc.202000068.
(27) Wieghold, S.; Bieber, A. S.; VanOrman, Z. A.; Nienhaus, L. Influence of Triplet Diffusion on Lead Halide Perovskite-Sensitized Solid-State Upconversion. *J. Phys. Chem. Lett.* **2019**, *10*, 3806−3811.
(28) Wieghold, S.; Bieber, A. S.; VanOrman, Z. A.; Daley, L.; Leger, M.; Correa-Baena, J.-P.; Nienhaus, L. Triplet Sensitization by Lead Halide Perovskite Thin Films for Efficient Solid-State Photon Upconversion at Subsolar Fluxes. *Matter* **2019**, *1*, 705−719.
(29) Nienhaus, L.; Correa-Baena, J.-P.; Wieghold, S.; Einzinger, M.; Lin, T.-A.; Shulenberger, K. E.; Klein, N. D.; Wu, M.; Bulović, V.; Buonassisi, T.; et al. Triplet-Sensitization by Lead Halide Perovskite Thin Films for Near-Infrared-to-Visible Upconversion. *ACS Energy Lett.* **2019**, *4*, 888−895.
(30) Ma, L.; Zhang, K.; Kloc, C.; Sun, H.; Michel-Beyerle, M. E.; Gurzadyan, G. Singlet Fission in Rubrene Single Crystal: Direct Observation by Femtosecond Pump−Probe Spectroscopy. *Phys. Chem. Chem. Phys.* **2012**, *14*, 8307−8312.
(31) Sutton, C.; Tummala, N. R.; Beljonne, D.; Brédas, J.-L. Singlet Fission in Rubrene Derivatives: Impact of Molecular Packing. *Chem. Mater.* **2017**, *29*, 2777−2787.

(32) Piland, G. B.; Burdett, J. J.; Kurunthu, D.; Bardeen, C. J. Magnetic Field Effects on Singlet Fission and Fluorescence Decay Dynamics in Amorphous Rubrene. *J. Phys. Chem. C* **2013**, *117*, 1224−1236.
(33) Zhang, Y.; Forrest, S. R. Triplets Contribute to Both an Increase and Loss in Fluorescent Yield in Organic Light Emitting Diodes. *Phys. Rev. Lett.* **2012**, *108*, 267404.
(34) Radiunas, E.; Dapkevicius, M.; Raisys, S.; Jursenas, S.; Jozeliunaite, A.; Javorskis, T.; Sinkeviciute, U.; Orentas, E.; Kazlauskas, K. Impact of t -Butyl Substitution in a Rubrene Emitter for Solid State NIR-to-Visible Photon Upconversion. *Phys. Chem. Chem. Phys.* **2020**, *22*, 7392−7403.
(35) Wei, D.; Ma, F.; Wang, R.; Dou, S.; Cui, P.; Huang, H.; Ji, J.; Jia, E.; Jia, X.; Sajid, S.; et al. Ion-Migration Inhibition by the Cation−π Interaction in Perovskite Materials for Efficient and Stable Perovskite Solar Cells. *Adv. Mater.* **2018**, *30*, 1707583.
(36) Mahboub, M.; Maghsoudiganjeh, H.; Pham, A. M.; Huang, Z.; Tang, M. L. Triplet Energy Transfer from PbS(Se) Nanocrystals to Rubrene: The Relationship between the Upconversion Quantum Yield and Size. *Adv. Funct. Mater.* **2016**, *26*, 6091−6097.
(37) Radiunas, E.; Raisys, S.; Jursenas, S.; Jozeliunaite, A.; Javorskis, T.; Sinkeviciute, U.; Orentas, E.; Kazlauskas, K. Understanding the Limitations of NIR-to-Visible Photon Upconversion in Phthalocyanine-Sensitized Rubrene Systems. *J. Mater. Chem. C* **2020**, *8*, 5525−5534.
(38) Fielitz, T. R.; Holmes, R. J. Crystal Morphology and Growth in Annealed Rubrene Thin Films. *Cryst. Growth Des.* **2016**, *16*, 4720−4726.
(39) Finton, D. M.; Wolf, E. A.; Zoutenbier, V. S.; Ward, K. A.; Biaggio, I. Routes to Singlet Exciton Fission in Rubrene Crystals and Amorphous Films. *AIP Adv.* **2019**, *9*, 095027.
(40) Piland, G. B.; Burdett, J. J.; Dillon, R. J.; Bardeen, C. J. Singlet Fission: From Coherences to Kinetics. *J. Phys. Chem. Lett.* **2014**, *5*, 2312−2319.
(41) Ryasnyanskiy, A.; Biaggio, I. Triplet Exciton Dynamics in Rubrene Single Crystals. *Phys. Rev. B: Condens. Matter Mater. Phys.* **2011**, *84*, 193203.

https://dx.doi.org/10.1021/acs.jpcc.0c05290
J. Phys. Chem. C 2020, 124, 18132−18140